J. Cent. South Univ. (2022) 29: 712−725
DOI: https://doi.org/10.1007/s11771-022-4943-7

Springer

Microseismic source location using the Log-Cosh function and distant sensor-removed P-wave arrival data

PENG Kang(彭康)[1], GUO Hong-yang(郭宏扬)[2], SHANG Xue-yi(尚雪义)[2]*

1. School of Resources and Safety Engineering, Central South University, Changsha 410083, China;
2. State Key Laboratory of Coal Mine Disaster Dynamics and Control, School of Resources and Safety Engineering, Chongqing University, Chongqing 400044, China

Abstract: Source location is the core foundation of microseismic monitoring. To date, commonly used location methods have usually been based on the ray-tracing travel-time technique, which generally adopts an L1 or L2 norm to establish the location objective function. However, the L1 norm usually achieves low location accuracy, whereas the L2 norm is easily affected by large P-wave arrival-time picking errors. In addition, traditional location methods may be affected by the initial iteration point used to find a local optimum location. Furthermore, the P-wave arrival-time data that have travelled long distances are usually poor in quality. To address these problems, this paper presents a microseismic source location method using the Log-Cosh function and distant sensor-removed P-wave arrival data. Its basic principles are as follows: First, the source location objective function is established using the Log-Cosh function. This function has the stability of the L1 norm and location accuracy of the L2 norm. Then, multiple initial points are generated randomly in the mining area, and the established Log-Cosh location objective function is used to obtain multiple corresponding location results. The average value of the 50 location points with the largest data field potential values is treated as the initial location result. Next, the P-wave travel times from the initial location result to triggered sensors are calculated, and then the P-wave arrival data with travel times exceeding 0.2 s are removed. Finally, the aforementioned location steps are repeated with the denoised P-wave arrival dataset to obtain a high-precision location result. Two synthetic events and eight blasting events from the Yongshaba mine, China, were used to test the proposed method. Regardless of whether the P-wave arrival data with long travel times were eliminated, the location error of the proposed method was smaller than that of the L1/L2 norm and trigger-time-based location method (TT1/TT2 method). Furthermore, after eliminating the P-wave arrival data with long travel distances, the location accuracy of these three location methods increased, indicating that the proposed location method has good application prospects.

Key words: seismic source location; Log-Cosh function; data field theory; location stability

Cite this article as: PENG Kang, GUO Hong-yang, SHANG Xue-yi. Microseismic source location using the Log-Cosh function and distant sensor-removed P-wave arrival data [J]. Journal of Central South University, 2022, 29(2): 712−725. DOI: https://doi.org/10.1007/s11771-022-4943-7.

Foundation item: Project(cstc2020jcyj-bshX0106) supported by the Chongqing Postdoctoral Science Foundation, China; Project (2020M683247) supported by the China Postdoctoral Science Foundation; Project(cstc2020jcyj-zdxmX0023) supported by the Key Natural Science Foundation Project of Chongqing, China; Project(551974043) supported by the National Natural Science Foundation of China;
Received date: 2020-12-24; **Accepted date:** 2021-05-21
Corresponding author: SHANG Xue-yi, PhD, Associate Professor; Tel: +86-18711050540; E-mail: shangxueyi@cqu.edu.cn; ORCID: https://orcid.org/0000-0003-0175-1853

1 Introduction

In recent years, considerable attention has been paid to engineering safety. Consequently, microseismic monitoring (e.g., mine engineering [1−3], tunnelling [4] and injection-induced seismicity [5]) is becoming increasingly popular in hazard early warning. Mine microseismic events are usually generated by cavity collapses, fault slips, or rock bursts [6]. Energy is transmitted in the form of stress waves, and a sensor is used to transform these stress waves into continuous voltage signals. This continuous voltage signal is then discretized, pre-processed (e. g., filtering) and stored by the NetADC, NetSP, and a data storage centre respectively. Finally, this signal is used to calculate the seismic source location, event magnitude, and source mechanism, which together provide a data basis for judging the stability of a rock mass [7, 8]. Microseismic monitoring technology includes sensor network optimization, data processing, and microseismic source location [8]. Among these, source location is the basis for subsequent processes such as seismic magnitude calculation, focal mechanism inversion, and hazard assessment. Therefore, research on microseismic source location has important applications. The location accuracy of microseismic events mainly depends on the source location objective function, inversion method, and quality of P-wave arrival data. We will briefly introduce the state-of-the-art source location research in terms of these three aspects.

To date, the most commonly used approach has involved travel-time-based ray-tracing location methods, which exploit the residual between the observed arrival time and theoretical arrival time (TT method) or the time difference between two sensors (TD method). In these methods, the L1 and L2 norms are usually adopted to construct the source location objective function. For example, DURAISWAMI et al [9] established the L1 norm-based TT location method (TT1 method), whereas DAI et al [10] proposed the L2 norm-based TD location method (TD2 method). Moreover, LI et al [11] and LI et al [12] listed the L1/L2 norm and TT/TD method combined four types of source location objective functions. They showed that the L1 norm is less affected by a large P-wave arrival picking error than the L2 norm, but its location accuracy is usually lower. The L2 norm has a high location accuracy but is easily affected by large P-wave arrival picking errors. Therefore, it is necessary to establish a source location objective function that has a high accuracy, for which the P-wave arrival data are of good quality and are not sensitive to large P-wave arrival picking errors.

The source location objective function is usually solved by applying gradient algorithms (e. g., the Quasi-Newton method [13]), which can rapidly identify the microseismic event location. However, gradient algorithms can be affected by the initial iteration value. For this reason, global search algorithms, such as the grid search technique, genetic algorithm, particle swarm algorithm, and Bayesian inversion [14], have also been adopted to solve the source location objective function. For example, NELSON et al [15] proposed a grid-search-based location algorithm that can be used for three-dimensional (3D) velocity structures. The grid search technique can usually find an approximate global optimal solution; however, it incurs a large computational cost [16]. The genetic algorithm has a relatively good global optimality, but its performance still depends on the selection of the initial values [14]. To address this, SONG et al [17] proposed a grid search and genetic algorithm jointed inversion method. This method first adopts a coarse grid search to find an approximate initial location and then applies a genetic algorithm to further improve the location accuracy. This combined technique has a lower calculation cost but higher location accuracy. However, all of the aforementioned location methods can still obtain local optimal solutions due to the effects of large P-wave arrival picking errors. Thus, we first aim to obtain multiple location points based on multiple initial points and then use the average of values with high location point densities as the location result. This can reduce the unstableness of a single time event location. In addition, the simplex method incurs a small computation cost but yields relatively good global optimality [18]. It can be combined with the aforementioned method to obtain multiple location points.

The source location is closely related to the

quality of P-wave arrival data. However, a mine microseismic signal can be affected by background noises (e.g., rock drilling and locomotive transportation), thereby reducing the picking accuracies of P-wave arrival times [19]. Moreover, mines have obvious high and low P-wave velocity zones due to the effects of geological conditions and mining activities. The velocity difference can reach up to 2000 m/s [20]. These high and low velocity regions cause obvious wavefront healing phenomena in the P-wave propagation path, i.e., the P-wave velocity outside the high speed region may be slower than that of the high velocity region [21]. In addition, microseismic waveform amplitudes attenuate with increasing travel distances. Therefore, the P-wave arrival amplitude may be very small and/or may be contaminated by noise. It can be inferred that when a P-wave travels for a long distance, there is likely to be a large difference between the observed arrival time and theoretical arrival time, thus affecting the seismic source location accuracy. For this reason, CHANG et al [22] analyzed the relationship between seismic waveform attenuation and travel distance. They used the TD method for adjacent seismic channels to calculate a microseismic event location, thus achieving a relatively small location error. Sensor array layouts in mines are generally relatively sparse, making it difficult to apply the approach of Ref. [22] to overcome the influence of the propagation path. Therefore, the P-wave arrival data corresponding to distant sensors should be excluded to ensure an accurate source location.

In this study, the following techniques are combined to improve microseismic location accuracy. First, a source location objective function is established based on the Log-Cosh function, which has the L2 norm advantage of high location accuracy for good P-wave arrival data and L1 norm stability when there are large P-wave arrival picking errors. Then, to reduce the influence of the initial value on the iteration algorithm, multiple initial points are randomly generated in the study area, and the simplex method is applied to calculate the location point corresponding to each initial point. Furthermore, the average value of 50 location points with the highest densities is selected as the initial source location; this improves the stability of the source location. Finally, to solve the problem of poor quality of P-wave arrival data from distant sensors, the aforementioned approximate location result is used to eliminate such P-wave arrival data. Then, the denoised P-wave data are used to obtain a high-precision location result.

2 Theoretical basis

2.1 Basic theory of travel-time-based location method

The velocity structures of mines are usually very complex, and most seismic source location methods treat them as homogenous velocity models [19]. We assume that the source coordinates are (x_0, y_0, z_0); source occurrence time is t_0; straight distance between the sensor and source is l_i; P-wave arrival time is t_i (i=1, 2, ⋯, n); n is the sensor number, and v_p is the P-wave velocity.

The P-wave travel time, which is based on the difference between the observed arrival time and source occurrence time, t_0, is calculated as follows:

$$\Delta t_1^i = t_i - t_0 \tag{1}$$

The theoretical P-wave travel time, based on a homogenous velocity model, is:

$$\Delta t_2^i = l_i / v_p \tag{2}$$

Therefore, the P-wave travel time difference between the observed travel time and theoretical travel time is:

$$\Delta t_{12}^i = \Delta t_1^i - \Delta t_2^i = t_i - t_0 - l_i / v_p \tag{3}$$

Furthermore, the trigger time objective functions of the source location based on the L1 norm, L2 norm, and the Log-Cosh functions are established as:

$$\text{Minimize TT1}(x_0, y_0, z_0, t_0) = \sum_{i=1}^{n} \left| t_i - t_0 - l_i / v_p \right| \tag{4}$$

$$\text{Minimize TT2}(x_0, y_0, z_0, t_0) = \sum_{i=1}^{n} \left(t_i - t_0 - l_i / v_p \right)^2 \tag{5}$$

$$\text{Minimize Log - Cosh}(x_0, y_0, z_0, t_0) = \sum_{i=1}^{n} \lg\left[\cosh\left(t_i - t_0 - l_i / v_p \right) \right] \tag{6}$$

The relationships between the travel time misfits and loss values of these three objective

functions are shown in Figure 1. The L2 norm has a low loss value when the fitting error of the L2 norm is small; thus, it can achieve a high location accuracy when good quality P-wave arrival data are used. The L1 norm has a smaller sensitivity to travel time misfits than that of the L2 norm. The Log-Cosh function's fitting loss has a similar trend to that of the L2 norm for good quality P-wave arrival data and the L1 norm for poor quality P-wave arrival data, which is conducive to location accuracy and stability.

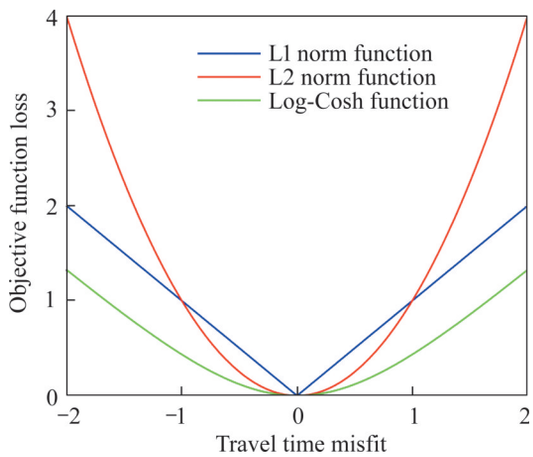

Figure 1 Relationship between travel time misfit and objective function loss

2.2 Data field theory

After generating multiple initial points and obtaining multiple corresponding location points, local optimizations may occur. This may, in turn, result in some differences between location points. However, most of these location points should be close to the true seismic event location. Therefore, it is necessary to apply an effective technique to characterise the point density. In this study, the data field theory proposed by WANG et al [23] was adopted to express the interactions between points in space. The more points there are around one point, the larger the data field potential value will be.

The potential value (scalar field intensity) of an object, x_i, in the data space can be defined as:

$$\varphi(x_i)=\sum_{j=1}^{n} m_j K\left(\left\|\boldsymbol{x}_i-\boldsymbol{x}_j\right\|/\sigma\right) \tag{7}$$

where $K(\cdot)$ is the unit potential function; $\left\|\boldsymbol{x}_i-\boldsymbol{x}_j\right\|$ represents the distance between objects $\boldsymbol{x}_i$ and $\boldsymbol{x}_j$; σ is the distance influence factor, which controls the interaction between objects; m_j represents the strength of object $\boldsymbol{x}_j$ on $\boldsymbol{x}_i$ in the data space; and n is the number of all location points.

To simplify Eq. (7), we assumed that each object has the same impact on x_i (i. e., m_j=1), $K\left(\left\|\boldsymbol{x}_i-\boldsymbol{x}_j\right\|/\sigma\right)$ is set to $\exp\left(-\left(\|\boldsymbol{x}_i-\boldsymbol{x}_j\|/\sigma\right)^2\right)$, and $\left\|\boldsymbol{x}_i-\boldsymbol{x}_j\right\|$ is set as the Euclidean distance between objects x_i and x_j. Equation (7) can then be converted to:

$$\varphi(\boldsymbol{x}_i)=\sum_{j=1}^{n}\exp\left(-\left[(x_i-x_j)^2+(y_i-y_j)^2+(z_i-z_j)^2\right]/\sigma^2\right) \tag{8}$$

where (x_i, y_i, z_i) and (x_j, y_j, z_j) are the 3D coordinates of the i-th and j-th location points, respectively.

2.3 Proposed method

A microseismic source location method is proposed using the Log-Cosh function and distant sensor-removed data. This method takes advantage of the Log-Cosh function for location accuracy and stability. Furthermore, it applies data field theory for characterising point density, considering that P-wave arrival-time data with long travel distances are usually poor in quality. The scheme of the proposed location method is shown in Figure 2. Its specific steps are as follows.

Step 1: The time difference between the observed arrival time-based travel time and the theoretical travel time is adopted to establish the Log-Cosh function-based source location objective function. This is calculated as shown in Eq. (6).

Step 2: Multiple location points are calculated for the seismic event.

Step 2.1: m points are randomly generated in the main mining area; these points follow a uniform distribution and are treated as the initial values of the simplex location method. For a small m, the corresponding location points may be relatively scattered, leading to a relatively bad location result based on the data field theory. A large m requires a large computation cost. We found that when m= 1000−2000, it yielded a good location result and an acceptable computation cost. Thus, m=2000 was adopted in this study, requiring approximately 5 s to calculate the location points by using parallel computation on two 18 core, 2.5 GHz CPUs.

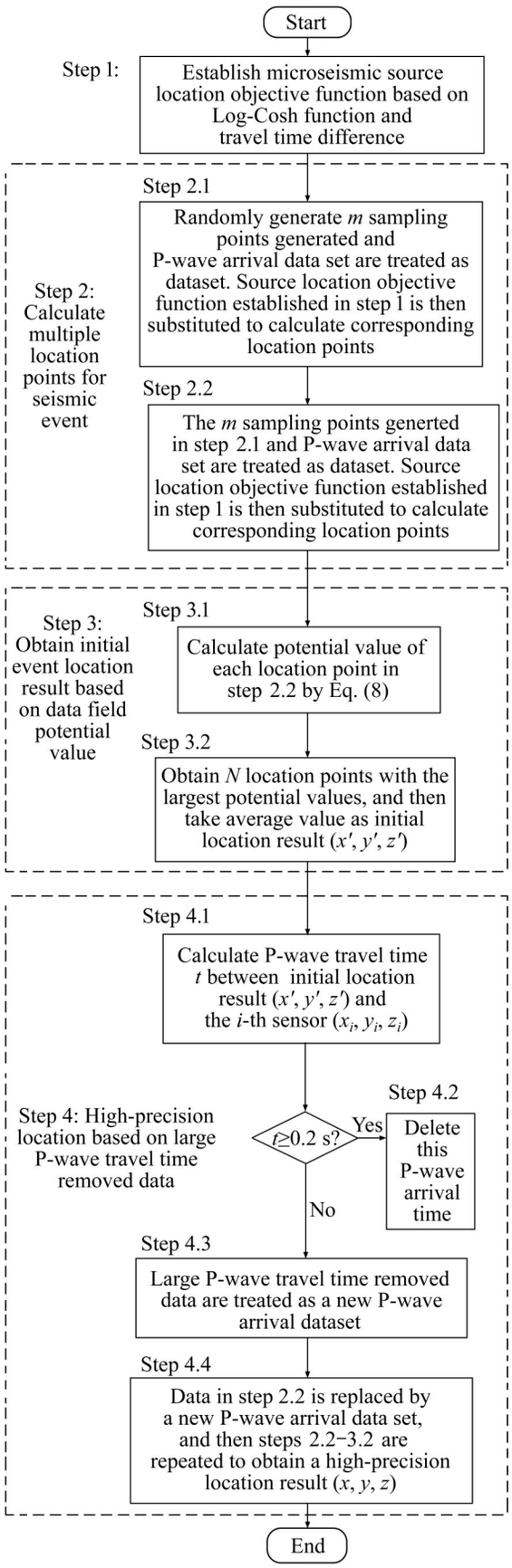

Figure 2 Flowchart of the mine microseismic source location method using the Log-Cosh function and large P-wave travel time removed data

Step 2.2: The initial points generated by using step 2.1 and the P-wave arrival data are treated as the dataset. They are then substituted into Eq. (6) as established in step 1, and the simplex method is used to solve this equation and obtain multiple location points.

Step 3: The intial event location result based on data field potential value.

Steps 3.1−3.2: The data field potential value of each location point is calculated by Eq. (8), and the average value of N (N=50) location points with the largest data field potential values is taken as the initial location result (x', y', z').

Step 4: High-precision location is obtained, without using data with large P-wave travel time.

Step 4.1: The P-wave travel time from the initial location result to each triggered sensor are calculated, and P-wave travel times that are larger than the threshold value (0.2 s) are removed. The threshold value is set according to Figure 13, which shows that when the P-wave travel time exceeds 0.2 s, it is likely to have a relatively large P-wave arrival picking error.

Steps 4.2−4.4: Steps 2.2−3.2 are repeated with the new P-wave arrival dataset to re-determine the location of the microseismic event (x, y, z); this is set as the final location result.

3 Synthetic test

The sensor locations and velocity model of the Yongshaba mine microseismic monitoring system (Section 4) in the Kaiyang city (Guizhou Province, China) were used for the basis of a synthetic test. Two events with locations inside and outside the sensor array were generated to test the effectiveness of the proposed location method. Their coordinates are (2997400 m, 381400 m, 1000 m) and (2997400 m, 381400 m, 1300 m). The locations of the sensors and the two test events are shown in Figure 3. The blue triangles show the sensor locations, whereas the red star represents the test event location. There are 28 sensors in this system, which are distributed at the levels of 930 m (12 sensors), 1080 m (12 sensors), and 1120 m (4 sensors). Field monitoring usually results in some un-triggered sensors, due to the influences of background noises, propagation distance, and sensor response. Therefore, we randomly selected 15

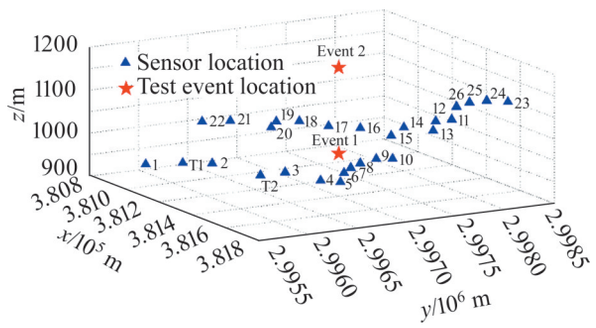

Figure 3 Spatial locations of sensors and synthetic events.

sensors from the 28 sensors to generate the theoretical P-wave travel time dataset. The P-wave velocity was set to 5200 m/s. The travel time was then obtained by dividing the distance by the P-wave velocity. As there were high and low velocity zones, and the picking of the P-wave arrival time can be affected by noise, errors usually occur in the picked P-wave arrival time. Thus, we added random noises following a 1 ms Gaussian distribution to each theoretical P-wave travel time. Furthermore, larger noises following a 5 ms Gaussian distribution were added to the P-wave travel time greater than 0.2 s. In addition, microseismic signals with severe amplitude attenuations, unstable arrival picking, and misclassification from different seismic events can result in a large P-wave arrival picking error. Thus, we also included a 50 ms picking error to one sensor. The relationship between travel distance and noisy P-wave travel times is shown in Figure 4. The red straight line represents the travel time−distance relationship at a velocity of 5200 m/s.

Based on the noisy P-wave travel time data of synthetic events 1 and 2, the location tests were performed by employing the steps described in Section 2.3. First, a uniform distribution function was used to randomly generate 2000 initial points in the main monitoring area, with $x\in$ (380900 m, 381800 m), $y\in$ (2995500 m, 2998500 m), and $z\in$ (900 m, 1150 m). Their coordinates and the P-wave travel time data were then substituted into Eq. (6). Finally, the simplex method was applied to obtain 2000 corresponding location points.

The 2000 location points of synthetic events 1 and 2 are shown in Figures 5 and 6, respectively. The black and red stars show the true and calculated

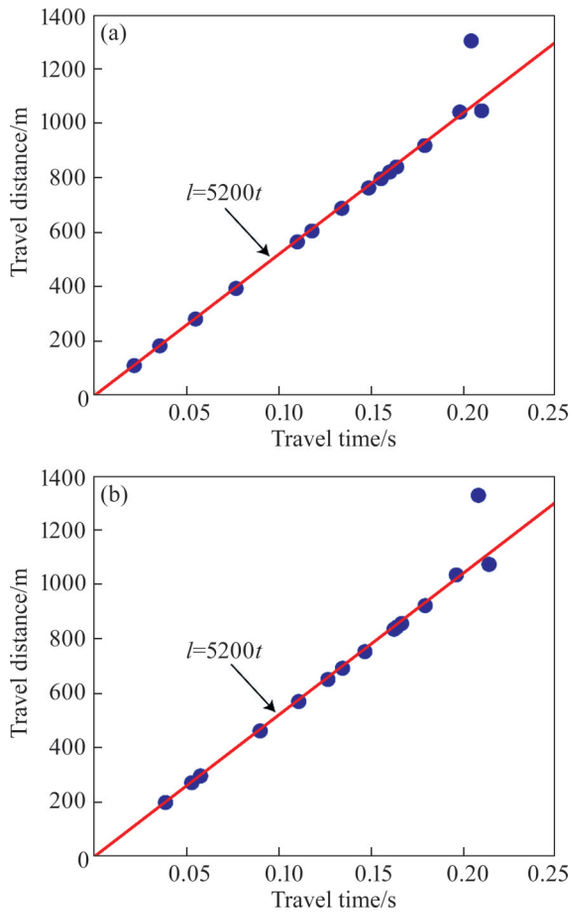

Figure 4 Relationship between P-wave travel distance and noisy P-wave travel time: (a) Synthetic event 1; (b) Synthetic event 2

locations, respectively. The circles show the 2000 location points, and their colors represent the magnitude of data field potential values. The 2000 location points of the data field and Log-Cosh function-based location method without removing the large P-wave travel times (DF1-Log-Cosh method) were more dispersed than those of the same method but with the large P-wave travel time data removed (DF1-Log-Cosh method). Furthermore, the DF2-Log-Cosh method exhibited a larger maximum potential value. When the synthetic event was inside the sensor array (synthetic event 1), the location errors of the DF1-Log-Cosh and DF2-Log-Cosh methods were 9.94 m and 8.74 m, respectively. For the synthetic event outside the sensor array (synthetic event 2), the location errors of the DF1-Log-Cosh and DF2-Log-Cosh methods were 17.31 m and 9.96 m, respectively. Therefore, although the data field could provide a stable approach for finding the event location, it was

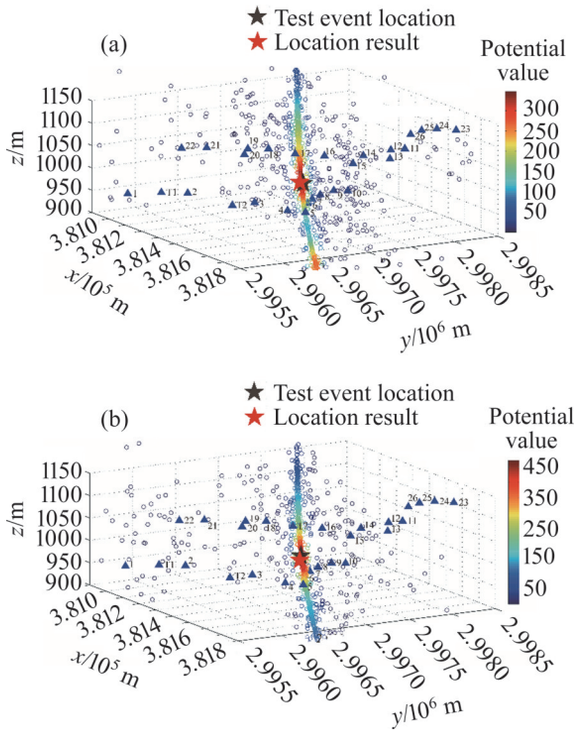

Figure 5 Log-Cosh function-based location results of synthetic event 1: (a) With large P-wave travel time unremoved; (b) With large P-wave travel time removed

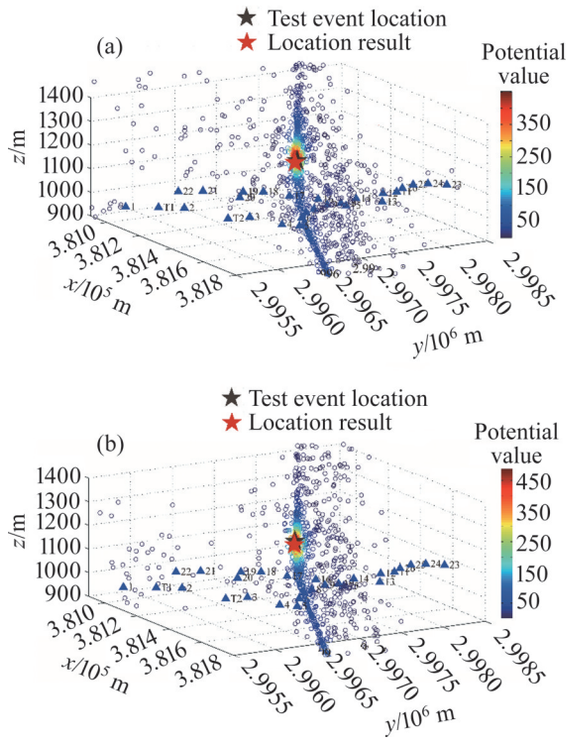

Figure 6 Log-Cosh function-based location results of synthetic event 2: (a) With large P-wave travel time unremoved; (b) With large P-wave travel time removed

necessary to eliminate those P-wave arrival data with long travel distances.

To further verify the effectiveness of the DF2-Log-Cosh method, we compared it with the DF1-TT1, DF2-TT1, DF1-TT2, and DF2-TT2 methods, where the only difference in each case was the objective function used, as shown in Eqs. (4)–(6). The location error boxplots of 2000 location points based on the TT1, TT2, and Log-Cosh objective functions are shown in Figure 7, and the data field-based final location results are listed in Table 1. The left and right sides of each boxplot group correspond to location results based on large P-wave travel time data unremoved and removed, respectively. The Log-Cosh function-based method generated more location points with small location errors when the large P-wave travel time data were not removed. This indicates the superiority of the Log-Cosh function. After eliminating the large P-wave travel time data, the location errors of each of these three location methods were reduced. The relative error reductions of the DF2-TT2 and DF2-Log-Cosh methods were more obvious. For the test event inside the sensor array, the Log-Cosh

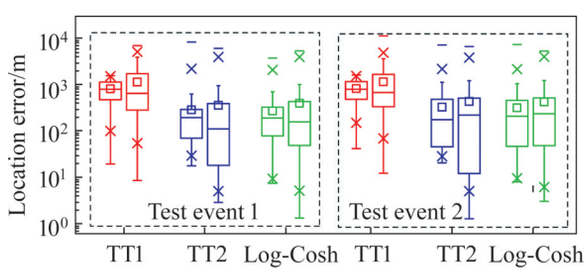

Figure 7 Location error boxplot of 2000 location points with different objective functions

function-based method returned more location points with small errors; this is beneficial in determining location result based on the data field theory. Moreover, when the P-wave arrival error was relatively small, the location result for the L2 norm method was better than that using the L1 norm-based location method. For the event outside the sensor array, the DF2-TT2 and DF2-Log-Cosh methods returned similar location results, both of which were much better than that of the DF2-TT1 method. Furthermore, the location errors of the DF1-Log-Cosh method for synthetic events 1 and 2 were 9.94 m and 17.31 m, respectively, both of which were lower than those produced by the

Table 1 Location results based on different objective functions

Event ID	Data	Location method	Location result			Location error/m
			x/m	*y*/m	*z*/m	
Synthetic event 1	All P-wave arrival time	DF1-TT1	381467.06	2997018.21	1039.13	79.75
		DF1-TT2	381372.96	2996983.96	1009.93	32.97
		DF1-Log-Cosh	381392.61	2996993.73	1002.19	9.94
	P-wave arrival time less than 0.2 s	DF2-TT1	381366.36	2997022.16	1045.09	60.46
		DF2-TT2	381407.37	2996999.33	992.35	10.64
		DF2-Log-Cosh	381406.63	2996999.37	994.34	8.74
Synthetic event 2	All P-wave arrival time	DF1-TT1	381307.11	2996741.79	1117.50	286.54
		DF1-TT2	381381.34	2996981.86	1236.23	44.61
		DF1-Log-Cosh	381395.92	2996992.59	1215.10	17.31
	P-wave arrival time less than 0.2 s	DF2-TT1	381240.96	2997018.33	1165.58	163.75
		DF2-TT2	381404.59	2996999.62	1191.35	9.80
		DF2-Log-Cosh	381404.33	2996999.67	1191.04	9.96

DF1-TT1 and DF1-TT2 methods. This could suggest that the Log-Cosh-based method is more likely to have a better location accuracy than the TT1 method when the P-wave arrival data are good. In addition, the Log-Cosh-based method exhibited a better location stability than the TT2 method under large P-wave arrival time errors. In addition, after removing the large P-wave travel time data, the DF2-TT1 method still obtained relatively bad location results, thereby verifying the low location accuracy of the TT1 based method. The TT2 method returned a good location result when supplied with good P-wave arrival data. The location errors of the DF2-Log-Cosh method for synthetic events 1 and 2 were only 8.74 m and 9.96 m, respectively. This indicates the necessity of eliminating large P-wave travel time data and the effectiveness of the Log-Cosh function-based location method.

Furthermore, we added noise to the travel time data of synthetic events 1 and 2 as defined earlier and generated 200 noisy P-wave travel time datasets. Then, we performed the same location processes as detailed earlier for these 200 datasets. The location error boxplots for datasets with and without large P-wave travel time errors are shown in Figure 8. The DF2-Log-Cosh function-based method returned the smallest average location error, whereas the L1 norm-based location result exhibited a relatively large average location error. This indicates that the DF2-Log-Cosh function and L2

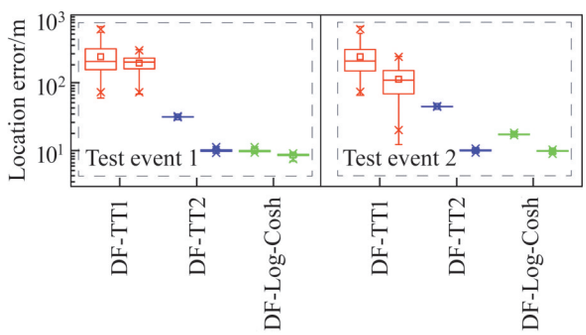

Figure 8 Location error boxplots of 200 P-wave travel time datasets based on different objective functions

norm may usually achieve better location results for datasets with relatively low noise. After removing the large P-wave travel time data, the TT2 norm and Log-Cosh function-based methods showed equal location performances. In conclusion, the DF2-Log-Cosh method can achieve a good location result.

4 Engineering applications

4.1 Engineering background

Eight blasting events recorded by the microseismic monitoring system of the Yongshaba mine, China, were selected to verify the proposed location method. In previous years, sublevel open-pit mining method was used in this mine, which resulted in the formation of several caves and may cause surface subsidence, roof collapse, and fault slip. These events can severely threaten mining safety. Therefore, an IMS microseismic monitoring system was developed at the site; it contains a data processing centre, a data exchange centre, eight

stations, and 28 sensors. The sensors were distributed at the levels of 930 m (12 sensors), 1080 m (12 sensors), and 1120 m (4 sensors) (Figures 3 and 9). The blue triangles and red stars represent the sensor and blasting event locations respectively, and the blue line connects each blasting event with its triggered sensor.

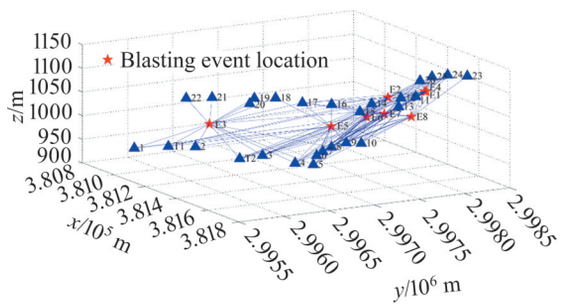

Figure 9 3D locations of 28 sensors and eight blasting events

4.2 Blasting event location test

The locations of the eight blasting events are listed in Table 2. Blasting events 6 and 3 were taken as examples. The P-wave arrival pickings of blasting event 6 are shown in Figure 10. Here, "#" indicates the sensor ID, where l is the linear distance between blasting event 6 and the corresponding sensor.

The microseismic waveforms were sorted according to the linear distance between the blasting event and each triggered sensor. The microseismic waveform amplitude and signal-to-noise ratio tended to decrease, and it was difficult to pick up the P-wave arrivals for the last few waveforms. This indicates that distant P-wave arrivals were likely to have low reliability.

The P-wave arrival pickings in Figure 10 were taken as the dataset, and the location method proposed in Section 2.3 was used to obtain the result shown in Figure 11. Similarly, the location result of blasting event 3 (Figure 12) was obtained by applying the same procedure. The location points of the DF1-Log-Cosh and DF2-Log-Cosh methods are shown in panels (a) and (b), respectively in each case. The 2000 location points of blasting event 6 were more concentrated than those of blasting event 3; this may be due to a better triggered sensor distribution for blasting event 6. Moreover, the 2000 location points in the vertical direction were mainly distributed in a straight line, which may be caused by insufficient vertical constraints regarding the existing sensor distribution. The 2000 location points in the DF1-Log-Cosh location method were relatively scattered, and their maximum potential value was smaller than that of the DF2-Log-Cosh location method. Furthermore, the DF1-Log-Cosh location errors of blasting events 6 and 3 were 73.91 m and 60.30 m, respectively when using all of the picked P-wave arrival data, whereas their DF2-Log-Cosh location errors were 51.70 m and 27.20 m, respectively. This again indicates the necessity of eliminating distant P-wave travel time data. It should be mentioned that the application location errors of blasting events 6 and 3 were larger than those of the synthetic tests, which could be a combined result of the heterogeneous velocity model and the larger P-wave arrival time errors of the blasting events. Here, the P-wave arrival time error originated from the signal propagation attenuation, P-wave arrival picking error, and delay

Table 2 Location results of eight blasting events based on DF-Log-Cosh method

Event ID	Measured location			Location result based on all P-wave arrival data				Location result based on P-wave arrival time less than 0.2 s			
	x/m	y/m	z/m	x/m	y/m	z/m	Error/m	x/m	y/m	z/m	Error/m
1	381683	2997760	1107	381647.67	2997787.39	1112.90	45.09	381647.83	2997787.36	1112.94	44.95
2	381653	2997405	1099	381611.34	2997403.04	1050.22	64.18	381625.25	2997399.21	1063.50	45.43
3	381194	2996224	1014	381166.99	2996245.35	964.50	60.30	381173.62	2996241.09	1008.28	27.20
4	381684	2997777	1107	381672.34	2997809.74	1117.09	36.19	381688.83	2997785.14	1129.75	24.64
5	381503	2997036	1028	381487.82	2996999.93	1030.42	39.21	381496.77	2997006.56	1029.23	30.12
6	381590	2997278	1053	381538.98	2997226.30	1066.71	73.91	381545.22	2997252.53	1048.61	51.70
7	381526	2997584	1044	381513.17	2997614.32	1048.36	33.21	381535.64	2997607.34	1051.84	26.45
8	381442	2998029	1017	381421.70	2998063.99	1024.14	41.08	381426.44	2998027.89	1053.85	40.02
Average							49.14				36.31

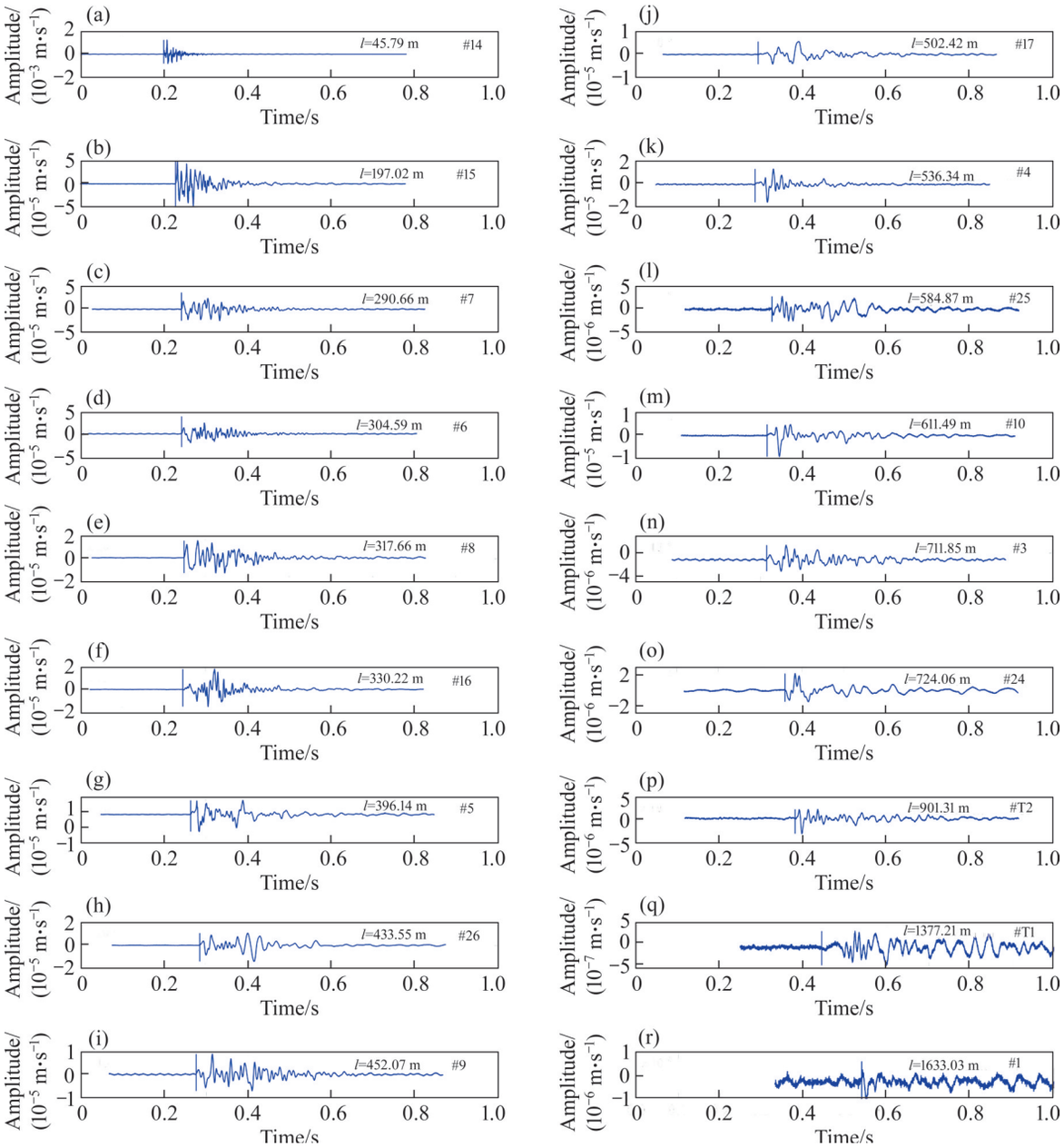

Figure 10 Microseismic waveforms (blue curves) and manual pickings (vertical lines) for blasting event 6

time difference from each sensor to the signal storage system.

The location results of the eight blasting events are listed in Table 2, and the relationship between the travel distance and travel time is shown in Figure 13. The source occurrence time, T_0, was taken as the median of the P-wave arrival time minus the blasting event location-based P-wave theoretical travel time, and the value was then set as the zero point. The P-wave velocity was used as the slope to obtain the straight blue line shown in Figure 13. The black circle is obtained from the distances between each blasting event and the sensor locations, whereas the blue (travel time is less than 0.2 s) and red (travel time is larger than 0.2 s) circles are obtained from the distances between the DF1-Log-Cosh location result and the sensor locations. The black circle was obtained from the distance between the blasting event and sensor locations, whereas the blue (travel time is less than 0.2 s) and red (travel time is larger than 0.2 s) circles were obtained from the distances between the DF1-Log-Cosh location results and the triggered sensors.

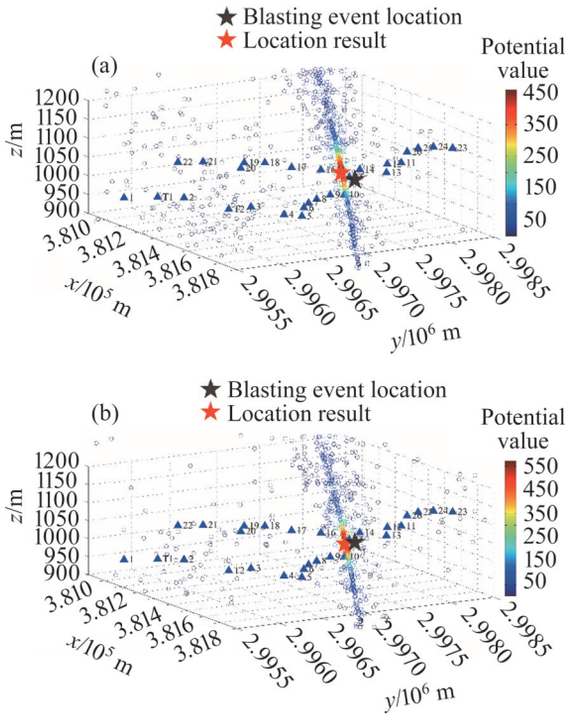

Figure 11 Log-Cosh function-based location results of blasting event 6: (a) With large P-wave travel time unremoved; (b) With large P-wave travel time removed

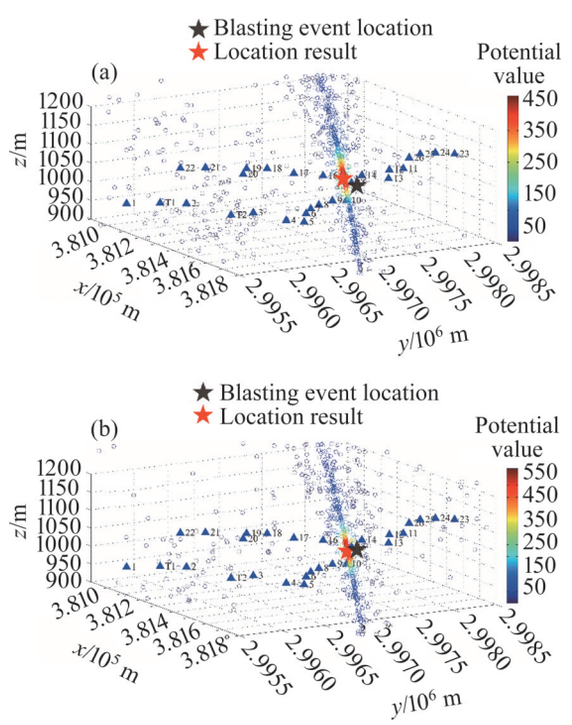

Figure 12 Log-Cosh function-based location results of blasting event 3: (a) With large P-wave travel time unremoved; (b) With large P-wave travel time removed

Generally, the closer a circle is to the blue line (Figure 13), the better the P-wave arrival time fitness is. Blasting events 1, 3, 5, and 6 exhibited poor fitness for large P-wave travel times, and their location errors, when including large P-wave travel time (t≥0.2 s) data, were 45.09, 60.30, 39.21, and 73.91 m, respectively. After removing the large P-wave travel times, the location errors of blasting events 3, 5, and 6 decreased to 27.20, 30.12, and 51.70 m respectively. Furthermore, the average location error of the eight blasting events decreased from 49.14 m to 36.31 m. Therefore, the DF2-Log-Cosh method, which eliminated distant P-wave travel time data, exhibited better location results.

5 Discussion

5.1 How to process poor P-wave arrival data

As mentioned earlier, the P-wave arrival can be affected by signal propagation attenuation, background noise, and signal misclassification, all of which may result in poor P-wave arrival pickings [24]. Poor P-wave arrival times can be removed by using the experienced time difference values between P-wave arrivals. For example, the P-wave arrival difference should be smaller than the largest travel time from one point to another within the study zone. However, poor P-wave arrival pickings generally cannot be removed from the aforementioned technique. To address this, LI et al [11] established an objective function in the form of exponential decay to reduce the influence of large P-wave arrival picking errors. However, a single time Newton iteration-based location result may be unstable. DONG et al [25] took advantage of the combination datasets from six sensors to obtain multiple location points. Then, they applied probability density curves in each direction to obtain an initial location result. They removed large P-wave arrival picking errors by using the initial location result-based P-wave travel time. Finally, they applied an iteration method to obtain the source location. However, when there are only a few triggered sensors, it is difficult to use probability density curves to obtain a good initial location result, and the single time relocation may still be affected by the initial iteration value. PENG et al [19] used bootstrap sampling to generate more P-wave travel time sub datasets. Then, they used the

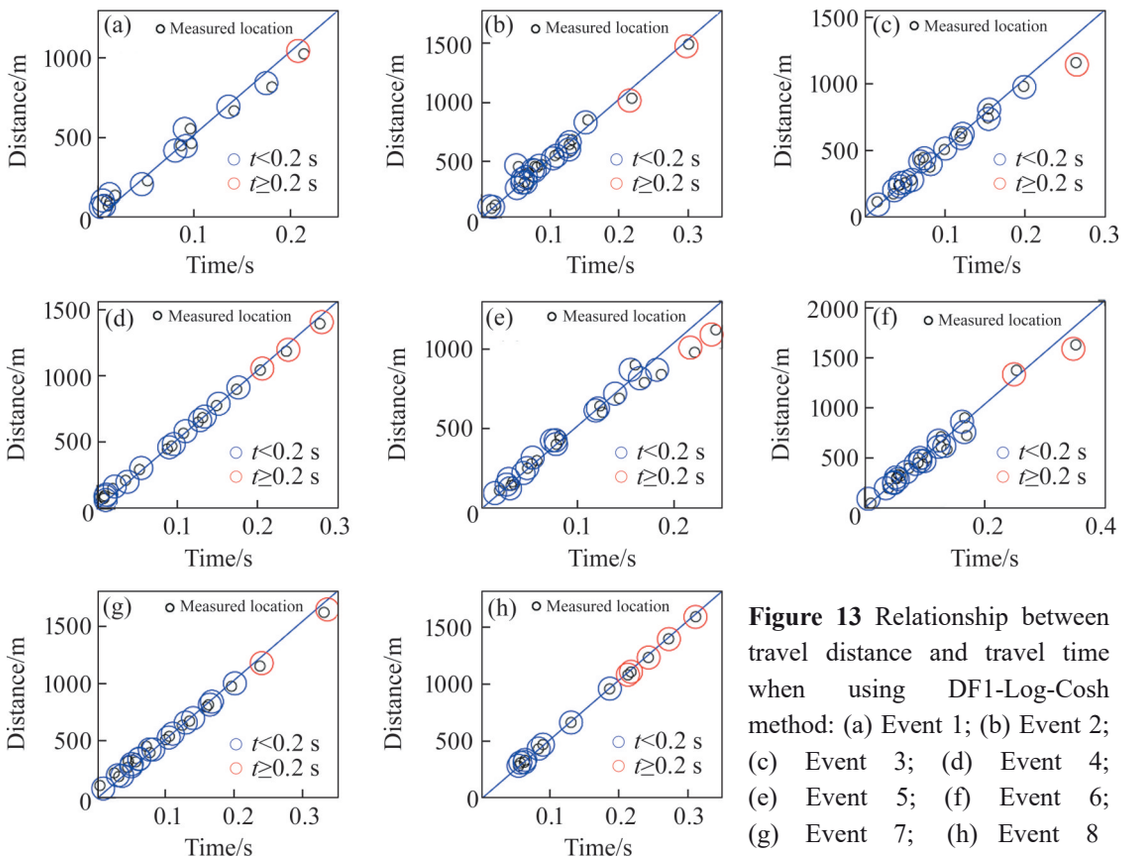

Figure 13 Relationship between travel distance and travel time when using DF1-Log-Cosh method: (a) Event 1; (b) Event 2; (c) Event 3; (d) Event 4; (e) Event 5; (f) Event 6; (g) Event 7; (h) Event 8

data field to characterise the high density location points. In this study, we adopted a data field to describe the density of each location point and then relocated the event using distant P-wave travel time removed data. This approach combines the advantages of the methods proposed Ref. [19, 25].

5.2 Effect of P-wave travel time modelling

We adopted a homogeneous velocity model to calculate the P-wave travel time. For a small zone, the P-wave propagation path can be treated as a straight line. Furthermore, the calculated travel time error is small compared with the real travel time. For a large zone, the ray path is not a straight line due to velocity variations [21], and the straight line based P-wave travel time may contain a relatively large error. Therefore, several studies have applied a 1D velocity model to calculate the ray travel time, which is better than a homogeneous velocity model. However, there is still a gap between this approach and the complex ray propagation paths that usually occur in mines. Recently, DONG et al [26] introduced the A* search algorithm into source location for a 3D structure containing a hole. PENG et al [27] and JIANG et al [28] combined the fast marching method (FMM) and a 3D velocity model (empty zone plus homogenous velocity model) for the purposes of microseismic source location. WANG et al [21] established a 3D velocity model-based ray-tracing-and-shooting method for a high-resolution velocity model. This method can obtain a good P-wave travel time. Furthermore, as the ray tracing method does not consider the influence of waveform attenuation, 3D wavefield modelling that considers the influence of waveform attenuation can be introduced to obtain a better P-wave travel time [29]. However, the 3D ray-tracing-based FMM method, shooting method, and wavefield modelling require high computation costs. Thus, it is difficult to combine them with the method proposed here. In the future, we can introduce reciprocity between the sensor and source location to generate a high-precision P-wave travel time database, which could then be combined with the DF2-Log-Cosh-based location method to obtain a better location accuracy.

6 Conclusions

1) A Log-Cosh function-based source location objective function was proposed, which solved the problem of L1 norm's low location accuracy and L2 norm's instability for large P-wave arrival picking errors. The synthetic results showed that when there were large P-wave arrival picking errors, the Log-Cosh function obtained smaller location error points, which is beneficial to data field-based location. After eliminating large P-wave travel time data, the Log-Cosh function obtained a location accuracy similar to that obtained by the TT2 method.

2) We used 2000 randomly generated initial points to obtain 2000 location points, and the average location of the 50 points with the largest data field potential values was used as the event location result. Two synthetic tests and eight blasting events showed that this technique can significantly reduce the influence of the initial iteration value and obtain a stable location result.

3) To handle the low quality data of large P-wave travel times, we performed the location test on data with and without large P-wave travel times. The average location error of the eight blasting events decreased from 49.14 m to 36.31 m when large P-wave travel-time data were removed. Furthermore, the travel times corresponding to closer sensors showed better fitness values than those of distant sensors, demonstrating that it is necessary to eliminate large P-wave travel time data.

Reference

[1] DONG Long-jun, TANG Zheng, LI Xi-bing, et al. Discrimination of mining microseismic events and blasts using convolutional neural networks and original waveform [J]. Journal of Central South University, 2020, 27: 3078 − 3089. DOI: 10.1007/s11771-020-4530-8.

[2] CAO Wen-zhuo, DURUCAN S, CAI Wu, et al. The role of mining intensity and pre-existing fracture attributes on spatial, temporal and magnitude characteristics of microseismicity in longwall coal mining [J]. Rock Mechanics and Rock Engineering, 2020: 53: 4139 − 4162. DOI: 10.1007/s00603-020-02158-4.

[3] CAO Wen-zhuo, DURUCAN S, CAI Wu, et al. A physics-based probabilistic forecasting methodology for hazardous microseismicity associated with longwall coal mining [J]. International Journal of Coal Geology, 2020, 232: 103627. DOI: 10.1016/j.coal.2020.103627.

[4] GONG Feng-qiang, WU Wu-xing, LI Tian-bin, et al. Experimental simulation and investigation of spalling failure of rectangular tunnel under different three-dimensional stress states [J]. International Journal of Rock Mechanics and Mining Sciences, 2019, 122: 1365 − 1609. DOI: 10.1016/j.ijrmms.2019.104081.

[5] CAO Wen-zhuo, SHI Ji-quan, DURUCAN S, et al. Evaluation of shear slip stress transfer mechanism for induced microseismicity at in Salah CO_2 storage site [J]. International Journal of Greenhouse Gas Control, 2021, 107: 103302. DOI: 10.1016/j.ijggc.2021.103302.

[6] GONG Feng-qiang, WANG Yun-liang, LUO Song. Rockburst proneness criteria for rock materials: Review and new insights [J]. Journal of Central South University, 2020, 27(10): 2793−2821. DOI: 10.1007/s11771-020-4511-y.

[7] WARPINSKI Norm. Microseismic monitoring: inside and out [J]. Journal of Petroleum Technology, 2009, 61(11): 80−85. DOI: 10.2118/118537-JPT.

[8] GE Mao-chen. Efficient mine microseismic monitoring [J]. International Journal of Coal Geology, 2005, 64(1, 2): 44−56. DOI: 10.1016/j.coal.2005.03.004.

[9] DURAISWAMI R, ZOTKIN D, DAVIS L. Exact solutions for the problem of source location from measured time differences of arrival [J]. Journal of the Acoustical Society of America, 1999, 106(4): 277−2277. DOI: 10.1121/1.427784.

[10] DAI Feng, GUO Liang, XU Nu-wen. Improvement of microseismic location based on an anisotropic velocity model [J]. Chinese Journal of Geophysics-Chinese Edition, 2016, 59(9): 3291−3301, 2016. DOI: 10.6038/cjg20160914.

[11] LI Xi-bing, WANG Ze-wei, DONG Long-jun. Locating single-point sources from arrival times containing large picking errors (LPEs): the virtual field optimization method (VFOM) [J]. Sci Rep, 2016, 6. DOI: 10.1038/srep19205.

[12] LI Nan, WANG En-yuan, GE Mao-chen. A nonlinear microseismic source location method based on Simplex method and its residual analysis [J]. Arab J Geosci, 2014, 7: 4477−4486. DOI: 10.1007/s12517-013-1121-0.

[13] LI Gao-ming, CHEN Jing-yi, HAN Mei. Accurate microseismic event location inversion using a gradient-based method [C]// The SPE Annual Technical Conference and Exhibition. San Antonio, Texas, USA, 2012. DOI: 10.2118/159187-MS.

[14] DONG Long-jun, ZOU Wei, SUN Dao-yuan. Some developments and new insights for microseismic/acoustic emission source localization [J]. Shock and Vibration in Deep Mining Science, 2019: 9732606. DOI: 10.1155/2019/9732606.

[15] NELSON G D, VIDALE J E. Earthquake locations by 3D finite difference travel times [J]. Bulletin of the Seismological Society of America, 1990, 80(2): 395−410.

[16] OYE V, ROTH M. Automated seismic event location for hydrocarbon reservoirs [J]. Computers & Geosciences, 2003, 29(7): 851−63. DOI: 10.1016/S0098-3004(03)00088-8.

[17] SONG Wei-qi, YANG Xiao-dong. A joint inversion combining the gridsearch algorithm and the genetic algorithm under solution-domain constraints for microseismic events [J]. Oil Geophysical Prospecting, 2011,

46(2): 259−266.
[18] SPENDLEY W, HEXT G R, HIMSWORTH F R. Sequential application of simplex designs in optimisation and evolutionary operation [J]. Technometrics, 1962, 4(4): 441−461.
[19] PENG Kang, GUO Hong-yang, SHANG Xue-yi. Data field application in removing large P-phase arrival picking errors and relocating a mine microseismic event [J]. Soil Dynamics and Earthquake Engineering, 2020, 139: 106359. DOI: 10.1016/j.soildyn.2020.106359.
[20] WANG Ze-wei, LI Xi-bing, ZHAO Da-peng, et al. Time-lapse seismic tomography of an underground mining zone [J]. International Journal of Rock Mechanics and Mining Sciences, 2018, 107: 136−149. DOI: 10.1016/j.ijrmms.2018.04.038.
[21] WANG Yi, SHANG Xue-yi, PENG Kang. Relocating mining microseismic earthquakes in a 3-D velocity model using a windowed cross-correlation technique [J]. IEEE Access, 2020, 8: 37866 − 37878. DOI: 10.1109/ACCESS.2020.2974762.
[22] CHANG Xu, LI Zheng, WANG Peng, et al. Micro-seismic location based on frequency attenuation compensation [J]. Acta Geophysica Sinica, 2018, 61(1): 250 − 257. DOI: 10.6038/cjg2018L0396.
[23] WANG Shu-liang, GAN Wen-yan, LI De-yi, et al. Data field for hierarchical clustering [J]. International Journal of Data Warehousing and Mining (IJDWM), 2011, 7(4): 43−63. DOI: 10.4018/jdwm.2011100103.
[24] LI Xi-bing, SHANG Xue-yi, MORALES-ESTEBAN A, et al. Identifying P phase arrival of weak events: The Akaike Information Criterion picking application based on the Empirical Mode Decomposition [J]. Computers & Geosciences, 2017, 100: 57−66. DOI: 10.1016/j.cageo.2016.12.005.
[25] DONG Long-jun, ZOU Wei, LI Xi-bing, et al. Collaborative localization method using analytical and iterative solutions for microseismic/acoustic emission sources in the rockmass structure for underground mining [J]. Engineering Fracture Mechanics, 2019, 210: 95−112. DOI: 10.1016/j.engfracmech.2018.01.032.
[26] DONG Long-jun, HU Qing-chun, TONG Xiao-jie, et al. Velocity-free MS/AE source location method for three-dimensional hole-containing structures [J]. Engineering, 2020, 6(7): 827−834. DOI: 10.1016/j.eng.2019.12.016.
[27] PENG ping-an, WANG Li-guan. Targeted location of microseismic events based on a 3D heterogeneous velocity model in underground mining [J]. Plos One, 2019, 14(2): e0212881. DOI: 10.1371/journal.pone.0212881.
[28] JIANG Ruo-chen, DAI Feng, LIU Yi, et al. Fast marching method for microseismic source location in cavern-containing rockmass: performance analysis and engineering application [J]. Engineering, 2021, 7(7): 1023 − 1034. DOI: 10.1016/j.eng.2020.10.019.
[29] WANG Yi, SHANG Xue-yi, PENG Kang, et al. Rock fracture monitoring based on high-precision microseismic event location using 3D multiscale waveform inversion [J]. Geofluids, 2020: e8825140. DOI: 10.1155/2020/8825140.

(Edited by ZHENG Yu-tong)

中文导读

基于Log-Cosh函数及剔除远距离传感器P波到时的矿山微震震源定位方法

摘要：震源定位是微震监测的核心基础。目前使用较多的射线走时追踪定位方法主要基于L1和L2范数建立震源定位目标函数。然而，L1范数定位精度较低，L2范数易受P波初至大拾取误差影响。此外，传统定位方法易受初始点影响而得到局部最优，远距离P波初至数据质量较差。为此，本文提出了一种基于Log-Cosh函数及剔除远距离传感器到时的微震震源定位方法，其基本原理为：首先，建立基于Log-Cosh函数的震源定位目标函数，其具有L1范数的稳定性和L2范数的定位精度；其次，在矿山开采区域随机生成多个初始点，使用已建立的震源定位目标函数得到相应的多个初定位点，再以初定位点中数据场势值最大的50个定位点坐标均值作为初定位结果，计算初定位结果到各触发传感器的P波传播时间，剔除传播时间大于0.2 s的P波初至数据；最后，以去噪后的P波初至数据集重复上述定位步骤，得到高精度定位结果。以开阳磷矿用沙坝矿两个理论测试事件和八次爆破事件为例展开定位研究。结果表明，不管是否剔除传播时间较大的P波初至数据，基于数据场的Log-Cosh法定位误差都小于传统TT1法和TT2法定位误差，而在剔除传播时间较大的P波初至数据后，三种定位方法的定位精度都有所提高，表明本文所提出的定位方法具有较好的应用前景。

关键词：震源定位；Log-Cosh函数；数据场理论；定位稳定性